Article type: Research Paper

Title: High surface area honeycomb-shaped carbon nanotube supports for BiVO$_4$ based solar water splitting

Author(s), and Corresponding Author(s): Sarah Jessl[1], Jan, Rongé[2], Davor Copic[1], Michael A. Jones[3], Johan Martens[2], Michael De Volder[1,*]

[1] University of Cambridge, Department of Engineering, Cambridge CB2 1PZ, United Kingdom

[2] KU Leuven, Leuven, Centre for Surface Chemistry and Catalysis, Celestijnenlaan 200F, 3001 Leuven, Belgium

[3] University of Cambridge, Department of Chemistry, Cambridge CB2 1EW, United Kingdom

Abstract

Advances in the synthesis and assembly of nanomaterials offer a unique opportunity to purposefully design structures according to the requirements of the targeted applications. This paper shows a process to create robust 3D carbon nanotubes (CNT) structures, which provide an electrically conductive support for nanoparticle coating. We describe a process to reliably fabricate robust honeycomb structures with walls made out of aligned CNTs. We present a design of experiment analysis of this fabrication process and discuss methods to coat these honeycombs with BiVO$_4$ for solar fuel applications. The proposed honeycomb structure allows for an efficient transport of electrons through the electrode, as well as an enhanced light-electrode interaction. Finally, we demonstrate that the developed CNT electrodes can survive harsh BiVO$_4$ synthesis conditions and can subsequently be used as photoelectrodes for solar water splitting.

---

[*] Corresponding author. Tel: 01223 338176. E-mail: mfld2@cam.ac.uk

1. Introduction

Carbon Nanotubes (CNTs) have been studied extensively over the past decades, resulting in a myriad of processes to assemble them into controlled superstructures such as yarns [1][2]–[4], sheets [5], vertically aligned arrays (CNT forests) [6], [7], and more complex 3D geometries [8]–[10]. These advances are important as the organisation and packing of CNTs greatly affects their mechanical and electrical properties [1], [11]. Further, the ability to control their geometry and surface chemistry allows to design complex hybrid nanoparticle structures to target a specific application. CNT forests are very attractive starting material for this because they show anisotropic properties resulting from their alignment and they can be patterned using lithographic methods [12]. However, the density of CNT forests is typically low and so is their mechanical stiffness and electrical conductivity; an efficient way to improve this is by elasto-capillary aggregation [10], [13]–[15]. Elasto-capillary aggregation refers to a process whereby the CNTs are brought into closer packing. It relies on capillary forces which arise during the drying of wet fibres to pull them into clumped, densely packed aggregates (similar to bundles formed in wet hair [16]). The way a substrate is exposed to the liquid influences the elasto-capillary aggregation, e.g. by directed immersion the direction of the aggregation can be influenced or by dipping, only the CNT tips get in contact with the solvent.[17] Applied to CNT forests, this process results in a 100-fold enhancement of Young's modulus [9], decrease in electrical resistance [13] [18], and transformation of the forest geometry [10], [13], [17]. Chakrapani et al.[7] showed a cellular foam formation by immersion of a CNT structure into solvent. The strong capillary forces during solvent evaporation cause shrinkage and crack formation in the CNT structures. Strong van der Waals forces hold the densified nanotubes together causing stable cellular structures. It was found that the micro-crack formation is induced by the drying of the structure and followed by further in-plane shrinkage and bending of the CNTs, which results then in the open cellular foam formation. This paper focusses on the targeted creation of honeycomb structures with vertically aligned CNT walls (see fig 1). These structures are interesting because they are mechanically robust, allow for a straight forward control of the microscale pore structure (honeycomb cell width), and straight electron transport though the aligned CNTs honeycomb walls which is advantageous in energy storage applications as shown for Li-ion batteries recently.[19] While several CNT honeycomb

2

fabrication and modelling methods have been reported previously [7], [9], [12], [20]–[23], we found that the parameter space that results in defect free large area honeycomb structures is limited. To further understand the relevant factors affecting the honeycomb structure and defects we performed a design of experiment (DoE) analysis of the patterns and heights of CNT forests that result in high quality honeycomb electrodes.

Further, we found that due to their mechanical stability CNT honeycombs can withstand harsh chemical modification processes such as hot casting. This process is used in this paper to coat the CNT surface with bismuth vanadate ($BiVO_4$) to create high surface area photoelectrodes for solar water splitting. $BiVO_4$ is a particularly interesting photocatalyst for water splitting, since it has both a narrow band gap of $\sim$ 2.4 eV[24]–[26] resulting in visible light absorption and a suitable valence band edge ($\sim$2.4 V vs. RHE) which provides a strong driving force for water oxidation by photogenerated holes [27], [28]. By coating a thin $BiVO_4$ layer on CNT honeycomb electrodes, the CNTs can be used as electron collectors to counteract the charge recombination [29]–[31]. This was confirmed by recent reports on hydrothermally synthesized CNT - $BiVO_4$ compounds that show higher transient photocurrent densities than $BiVO_4$ by itself [32][31][33]. However, these previous reports are relying on CNT powders rather than structured CNT scaffolds as proposed in this work. This approach allows for a rational design of the electron transport as well as the pore structure of the electrode to improve its light harvesting performance and the flow of reagents in the electrode.

2. CNT Synthesis

As illustrated in Figure 1, a catalyst pattern is first patterned on the Si wafers using UV photolithography, followed by e-Beam evaporation of a catalyst layer for CNT growth (1 nm Fe – 10 nm Al_2O_3), and lift-off (see methods). This layer is then used in a chemical vapor deposition (CVD) process to grow vertically aligned CNT structures (Figure 1, step A). This is followed by a UV-ozone treatment to remove the tangled top layer of the CNT forest which would adversely affect the elastocapillary aggregation of the CNTs in the next step [34]. Here, the CNTs are capillary aggregated by applying a drop of acetone on the substrate. During the evaporation of the solvent, elastocapillary forces pull the CNTs closer together, changing the shape of the structure from circular holes (Figure 1c, left) into honeycombs (Figure 1c, right) [9], [12], [17], [35]. This CNT honeycomb structure is then coated with bismuth vanadate ($BiVO_4$) as a photocatalyst. This was pursued using a range of different microwave-assisted protocols as well as hotcasting (Figure 1e).
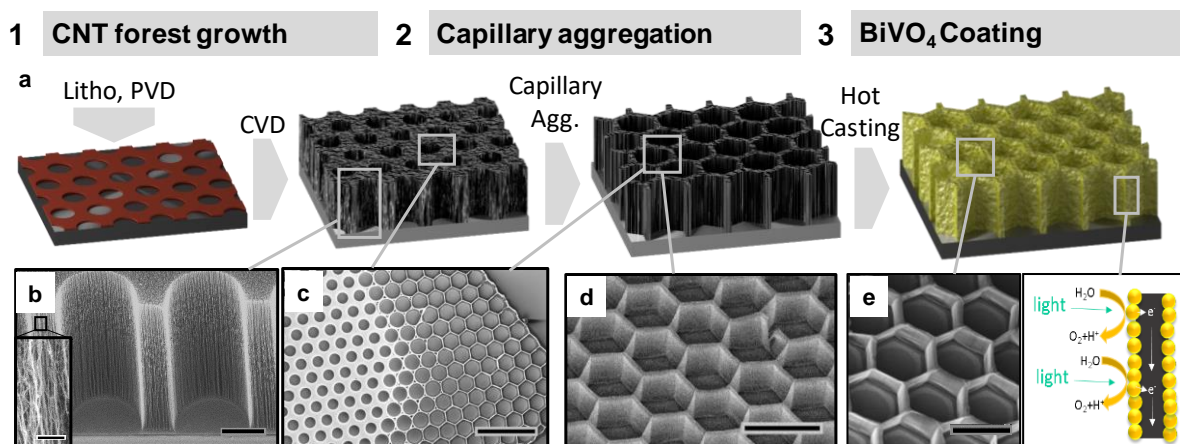
1 CNT forest growth   **2 Capillary aggregation**   **3 BiVO₄ Coating**

Figure 1. *The process flow for the honeycomb formation. (a) Schematics process steps. (b) SEM images of the as grown CNT forest using a chemical vapor deposition (CVD) process from a patterned catalyst film. (c,d) Elastocapillary aggregation of the CNTs re-shapes the circular patterns into honeycombs (left: as-grown forest with patterned holes - right: aggregated CNT structure). (e) Hot casting of a photocatalytic BiVO₄ coating. Scale bars in the SEM images are 300 nm in the inset in (b), 20 µm in (b), 40 µm in (e) and 100 µm in (c,d).*

3. Design of experiments

The main failure mode in the above process for fabricating CNT honeycombs is cracking of the honeycomb walls. These cracks seem to form at the top of the walls and propagate downward to the substrate, which is probably due to tension in the wall plane accrued during densification. Once a crack is formed, we observed an increased likelihood in cracks in the opposite wall, which may be due to increased loads on that wall as the opposite part of the cell detaches. This may lead to cascading failure of parallel walls of adjacent honeycombs (see Figure 2). Such large cracks make samples unsuitable to applications where the periodicity of honeycombs is of importance. Thus, we focussed on investigating the factors affecting crack formation, including hole diameters on the mask pattern (5, 10, 15, and 20 µm), catalyst width between holes (referred to as spacing, 5 and 10 µm), and CNT height (growth times of 2, 4, and 6 minutes).Three examples of the hole diameters and spacing can be seen in **Figure 2**a. In total, 54 experiments were conducted with 2 repetitions for each condition. For all those experiments the CVD synthesis temperature was fixed to 720 °C. The percentage of the cracked

area on a densified sample was determined by analyzing representative top-down SEM images using ImageJ. A threshold was applied to the SEM images, such that the area of the honeycomb cells (exposed substrate in top-down view) and that of groups of adjacent cracked honeycomb cells could be quantified. The total area of cracked honeycomb cells calculated as a percentage of the overall area is referred to herein as the "Crack Percentage". This procedure is carried out for the above range of diameter and spacing combinations. The results can be seen in **Figure 2**b as a colour map with some example SEM images. The colour is indicative of the percentage of cracks in the structure: green means there are less than 10% cracks, whereas red means the crack percentage is higher than 50%.
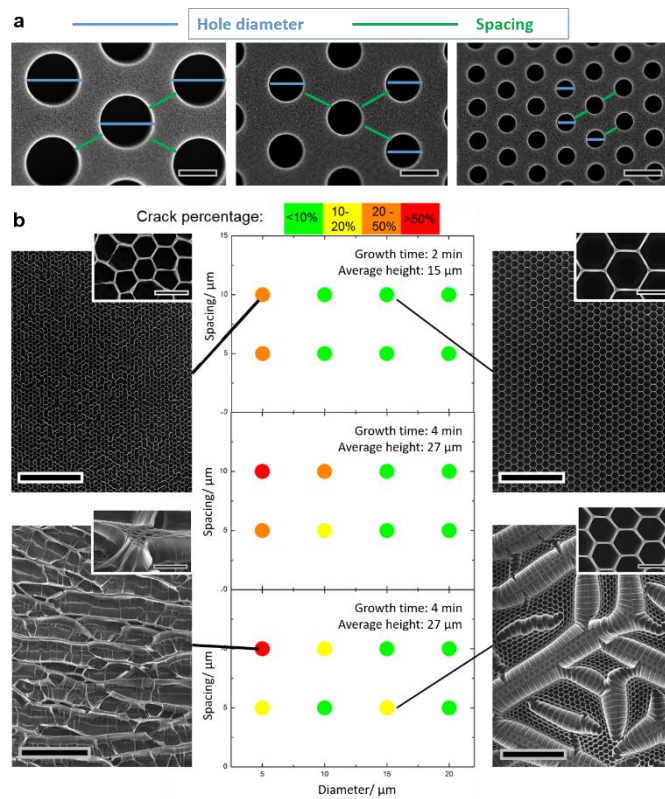

Figure 2. (a) Examples for different hole diameters and spacings on the used substrates. Scale bars are 10 μm. (b) The graphs show a color map of the percentages of the cracked areas as a function of the diameter and spacing of the circular hole pattern used to form the honeycomb structures and with an increasing growth height from the top graph to the bottom one. Additionally, SEM images as examples for each of the crack percentage ranges are provided. As the growth height depends on the growth time, the used height is an average of all the samples (18 samples) grown for the same time. Scale bars are 200 μm and 20 μm in the insets.

Figure 2b illustrates how the mean percentage of cracks or defects after capillary densification is influenced by the forest geometry. Depending on the initial geometry of the as-grown CNT forest, we found that the honeycombs can be defect free, or have substantial defects as illustrated in Figure 2b lower left. Overall, the percentage of the cracked area tends to be lower for larger diameters and larger spacings. This graph gives a first indication of factors affecting the fabrication of high quality honeycomb structures, but it also shows that there might be interdependencies among the individual factors, meaning that growth time, diameter, and spacing may have statistically significant interactions. To investigate this a 2-level full factorial regression design was implemented in Minitab, with diameter (5 and 20 µm), spacing (5 and 10 µm), and growth time (2 and 6 min) as factors (2 replicates per run). The computed analysis of variance (ANOVA) tables, regression models, and standardized effects plots are provided in the SI, showing the impact of the factors and their interactions on crack percentage, height, and wall thickness.

For the subsequent analysis a significance level of 0.10 is used (p-values provided in SI). Wall thickness is found to statistically depend on and to be increased by increasing the spacing and decreased by increasing diameter and all its interactions (denoted as diameter*spacing, diameter*growth time, and diameter*spacing*growth time). Height is found to only depend on growth time. Two responses for cracks are considered, namely percentage of undamaged cells and percentage of top down area that contains cracks that spread over 2 and up to 5 honeycomb cells. All factors and interactions are found to be statistically significant in affecting the percentage of undamaged honeycombs. Maximizing the percentage of undamaged cells can be accomplished by minimizing the growth time, spacing, and the spacing*growth time second order term, while maximizing all other terms and interactions. Lastly, the percentage of cracks that cross over 2 and up to 5 honeycomb cells can be reduced by decreasing the diameter and growth time. With the statistically significant factors and interactions identified and constructed regression models future honeycomb designs can have significantly reduced cracked cells and optimized heights and wall thicknesses.

4. BiVO₄ Coating

The process parameters allowing for large area reliable fabrication of CNT honeycombs (30 µm and a spacing of 10 µm, grown to a height of ~ 35 µm) are then used as scaffolds for $BiVO_4$ coating. Here we have both investigated a microwave-assisted, hydrothermal synthesis and a hot casting method. The hydrothermal process followed here was adapted from Shang et al.[36] (see experimental section), however, it did not enable uniform nucleation of particles

on the CNT honeycombs (see Figure S1a and b). Uniform films offer higher active surface areas and prevent undesired side reactions with bare CNTs. Additionally, XRD measurements showed that the particles had the wrong composition (see Figure S1c). Similar challenges were found using a protocol adapted from Liu et al.[37] (see experimental section). Here we found mostly homogeneously nucleated particles in the solution, rather than heterogeneous nucleation on the CNT walls (Figure S2d-f). Also these particles did not show m-BiVO4 in the XRD pattern (Figure S2c). Finally, a protocol adapted from Ma et al.[38], provided the desired phase of BiVO$_4$ (Figure S3), but again resulted in homogeneous rather than heterogeneous nucleation, and the material deposited on the CNTs suffered from flaking. Several other hydrothermal synthesis methods reported in literature are relying on HNO$_3$ which is incompatible with our CNT honeycombs. The above experiments illustrate the challenges in adapting synthesis protocols to work in conjunction with patterned CNT electrodes.

Given the above challenges with hydrothermal modification of the CNT honeycombs, a hot casting method was developed for this process based on previous work [24], [27]. The precursors are dropcasted onto the CNT honeycomb structure and the hotplate is heated to 350 ˚C for the solvent to evaporate. After cooling, an annealing step (2h at 500˚C in a helium atmosphere) is done to convert the particles to m-BiVO$_4$. In this process, we found that HNO$_3$ based protocols did not affect the CNTs much, probably due to the short (< 2 min) process time (see Figure 3b). In our process, bismuth nitrate pentahydrate and vanadium oxide are dissolved in 2M HNO$_3$ as precursors for the hotcasting, which result in the desired uniform coverage of the CNT honeycombs (Figure 3b,c). XRD measurements show that the coating is a monoclinic BiVO$_4$ phase (Figure 3d). Also Raman spectra (Figure 3e) show the symmetric stretching mode of VO$_4$ at 816 cm^{-1}, the asymmetric stretching mode at 698 cm^{-1}, the symmetric bending mode at 336 cm^{-1} and the asymmetric bending mode at 330 cm^{-1}, as reported in the literature for BiVO$_4$ [8],[9]. The Si-peak is attributed to the Si-wafer substrate. Finally, to further improve the electron transport in the electrodes, the CNT-structure is coated with an Au/Pd-layer prior to the hot casting process. A cleaved electrode was investigated using SEM and EDX (Figure S4, S5). This analysis did not show any clear layers of elements indicating a uniform coating with a mixture of Au/Pd and BiVO4 over the whole of the CNT structure.
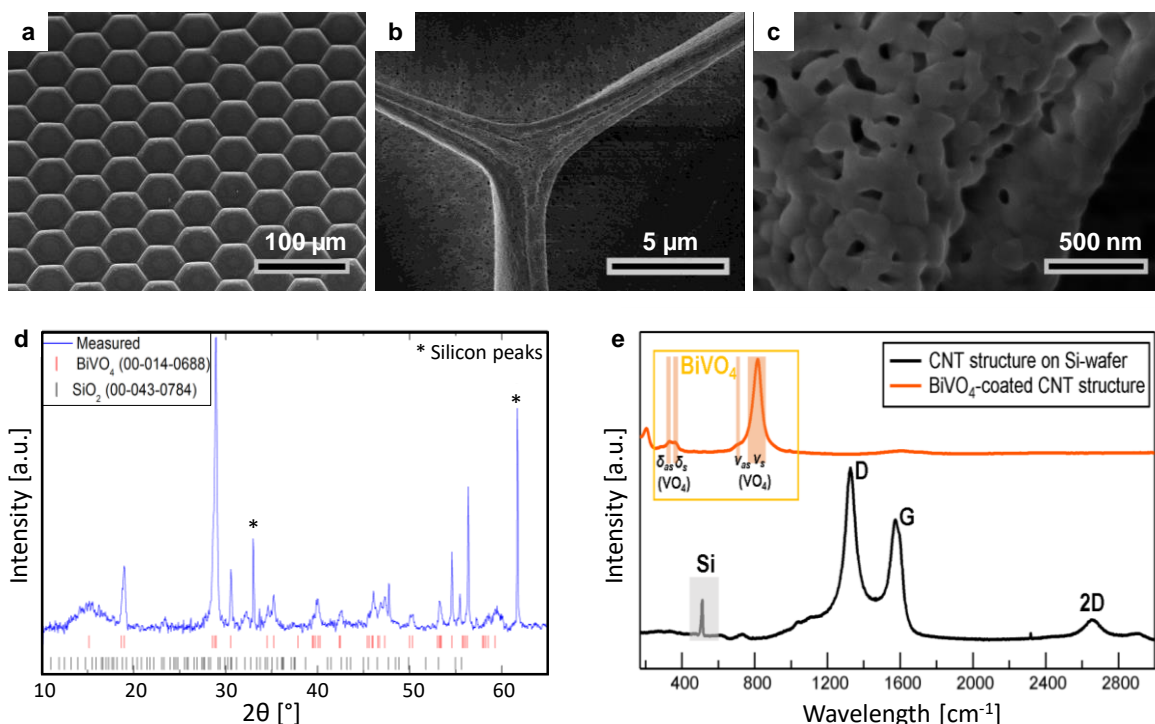
Figure 3. *A coating with precursors in nitric acid leads to no damage of the overall CNT honeycomb structure (a) and a uniform coating on top (b) and on the side walls (c). The XRD (d) shows substrate peaks (SiO$_2$) but otherwise no other phase than monoclinic BiVO4, making this a successful protocol for the formation of BiVO$_4$ particles on CNTs. The Raman spectrum (e) shows the emerging of VO$_4$ bending and stretching modes as well as the disappearing of the D, G and 2D peak due to coating of the substrate.*

5. Photocatalytic Performance

The above CNT-BiVO$_4$ honeycombs are then characterized as photoelectrodes for water splitting. A three-electrode configuration with graphite as a counter electrode and Ag/AgCl as a reference electrode is used. The electrolyte was 0.5 M potassium phosphate buffer (pH 6.8) with 0.5 M sodium sulfite (Na$_2$SO$_3$) as a hole scavenger to determine the efficiency of the BiVO$_4$ photoelectrode for generating and separating charge carriers upon radiation. Cyclic voltammetry (CV, Figure 4a and b) and chronoamperometry (CA, Figure 4b) measurements are performed for the characterization. The potential range is scanned while measuring the current (under illumination and in the dark) to determine the performance of the material. Additional CV measurements can be found in S6 (exceptionally good performance) and S7 (delamination of CNTs from sample).

The CV measurement (Figure 4a and b) shows a current density that responds to light (orange line). The photocurrent at 1 V vs RHE is ~0.07 mAcm^{-2}. When CA measurements are done at

1 V vs. RHE (figure 4c), a clear change with light can be detected in the current. The measured photocurrent is slightly lower at 0.065 mAcm^{-2}, which is expected due to transient effects. The observed photocurrent is lower than state of the art doped $BiVO_4$ photoelectrodes [41]–[43], but similar to non-optimized, non-doped materials [44]. The late photocurrent onset indicates a low photovoltage, due to inefficient charge separation. This could be improved via optimizing the film thickness and composition [44], for instance by varying coating process parameters such as the concentration of the solution.
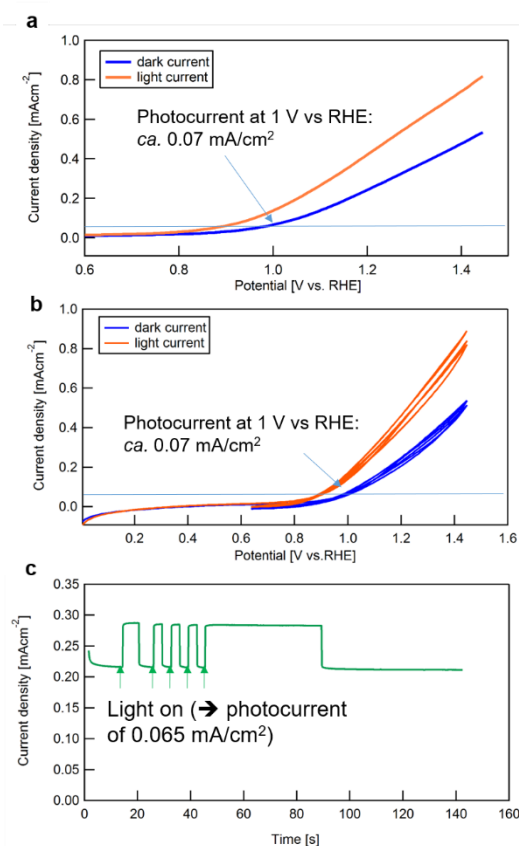

Figure 4. *Three-electrode measurements of BiVO₄-CNT sample in neutral phosphate buffer with sulphite hole scavenger. (a) The first cycle at 100 mV/s ,(b) Cyclic voltammetry at 100 mV/s, in the dark and under irradiation. (c) Chronoamperometry at 1 V vs RHE applied voltage, under chopped light conditions. An improvement of the current can be seen under irradiation.*

6. Conclusions

Honeycombs are found in many natural systems and engineering designs because of their unique mechanical properties. In this paper, we present a reliable fabrication process for honeycomb structures with walls made out of vertically aligned CNTs has been developed. The fabrication parameters affecting the quality of the CNT honeycombs have been analyzed using

DoE, and regression models are constructed to minimize the percentage of cracked honeycomb. The developed structure is very promising for a range of applications that need electrical conductivity, mechanical robustness, large surface area or high porosity. Here, this structure was used as a photocathode for which we explored a range of different $BiVO_4$ hydrothermal and hotcasting coating methods. We found that the CNT honeycombs can withstand these harsh synthesis conditions and deliver 0.065 $mAcm^{-2}$ in our setup.

7. Experimental Section

Patterning of catalyst for CNT growth. The catalyst is prepared on a silicon by standard photolithography up to the resolution limit of the employed slide mask (1.8 µm). An adhesion promoter (Ti-prime), positive photoresist (AZ 5214E) and developer (AZ 351B) is used for the photolithography. After templating the Si-wafer with either photoresist or PS-particle monolayers, the catalyst is deposited onto the wafer using an e-beam physical vapor deposition (PVD) system (Lesker). The catalyst deposited is a 10 nm Alumina (Al_2O_3, 1 $Ås^{-1}$), followed by a 1 nm Iron-layer (Fe, 0.25 $Ås^{-1}$). After the photoresist is lifted off, the catalyst is patterned.

CNT growth. For the growth of vertically aligned CNTs (VA-CNTs), an atmospheric pressure tube furnace is used. The standard procedure for the growth is an annealing time of 15 minutes under helium (100 sccm) and hydrogen (400 sccm) gas stream, then ethylene (100 sccm) is introduced. The time ethylene flows (= growth time) and the temperature of the furnace is used to control the forest height. The samples are grown at a temperature of 720 ℃ for 5 minutes. After the growth time the tube is pulled out of the furnace allowing the substrates to cool down for 2 minutes while the ethylene and hydrogen are still flowing.

CNT densification. The grown CNT structures are turned into CNT honeycomb structure by putting a drop of acetone on top of the grown structure. The acetone evaporation causes elastocapillary self-aggregation and thus forms the CNT honeycombs.

$BiVO_4$ hotcasting. 0.05 M Bismuth nitrate pentahydrate ($Bi(NO_3)_3 \cdot 5H_2O$, Sigma-Aldrich) and 0.05M vanadium oxide (V_2O_5, Aldrich) are dissolved in 2M HNO_3 as precursors for the hotcasting. The precursor solution are subsequently put onto the sample on a hotplate. Then the hotplate is heated to 350 °C and the solvent is evaporated. To finalize the BiVO4 crystallization, the sample is annealed at 500 °C for 2 hours with helium flowing at 350 sccm with a ramp rate of 10 °C/min.

Photoelectrode measurements. A three-electrode configuration with graphite as a counter electrode and Ag/AgCl as a reference electrode was used with 0.5 M sodium sulfite (Na2SO3) and 0.5 M KPi buffer (pH 6.8), with a 400 W Xe lamp with an AM 1.5 filter calibrated at 1

sun. The cell was stirred and purged with a moderate oxygen gas flow. No correction was made for uncompensated resistance losses.

Characterization. SEM measurements are taken using a Leo 1530VP Gemini from Zeiss operating at an accelerating voltage of 8 keV and using an InLens-detector. Samples are not sputtered with a metal layer. The XRD-system used is a D8- B1- Gen10 Bruker XRD. Measurements are done with a stepsize of 0.05 °(2θ), and a step time of 0.5 s. The software X-Pert Highscore Plus is used for the data evaluation. Raman measurements are done using a Bruker Senterra equipment with a 532 nm laser.

Conflict of Interest

The authors declare no conflict of interest.

SI

Supporting information is available or from the author.

Bibliography

[1]   M. F. L. De Volder, S. H. Tawfick, R. H. Baughman, and A. J. Hart, "Carbon nanotubes: present and future commercial applications," *Science (80-.).*, vol. 339, no. 6119, pp. 535–9, Feb. 2013.

[2]   M. Zhang, K. R. Atkinson, and R. H. Baughman, "Multifunctional carbon nanotube yarns by downsizing an ancient technology.," *Science (80-.).*, vol. 306, no. 5700, pp. 1358–1361, 2004.

[3]   K. Koziol *et al.*, "High-performance carbon nanotube fiber.," *Science*, vol. 318, no. 5858, pp. 1892–1895, 2007.

[4]   L. M. Ericson *et al.*, "Macroscopic , Neat , Single-Walled Carbon Nanotube Fibers,"

Science (80-.)., vol. 305, no. September, pp. 1447–1450, 2004.

[5]   M. Zhang *et al.*, "Strong, transparent, multifunctional, carbon nanotube sheets.," *Science (80-.).*, no. August, pp. 1215–1220, 2005.

[6]   K. Hata, D. N. Futaba, K. Mizuno, T. Namai, M. Yumura, and S. Iijima, "Water-assisted highly efficient synthesis of impurity-free single-walled carbon nanotubes.," *Science (80-.).*, vol. 306, no. 5700, pp. 1362–1364, 2004.

[7]   N. Chakrapani, B. Wei, A. Carrillo, P. M. Ajayan, and R. S. Kane, "Capillarity-driven assembly of two-dimensional cellular carbon nanotube foams.," *Proc. Natl. Acad. Sci. U. S. A.*, vol. 101, no. 12, pp. 4009–4012, 2004.

[8]   M. De Volder, S. Park, S. Tawfick, and J. A. Hart, "Strain-engineered manufacturing of freeform carbon nanotube microstructures.," *Nat. Commun.*, vol. 5, p. 4512, 2014.

[9]   M. De Volder *et al.*, "Diverse 3D microarchitectures made by capillary forming of carbon nanotubes," *Adv. Mater.*, vol. 22, no. 39, pp. 4384–4389, 2010.

[10]   D. N. Futaba *et al.*, "Shape-engineerable and highly densely packed single-walled carbon nanotubes and their application as super-capacitor electrodes," *Nat. Mater.*, vol. 5, no. December, pp. 987–994, 2006.

[11]   E. R. Meshot *et al.*, "Quantifying the Hierarchical Order in Self-Aligned Carbon Nanotubes from Atomic to Micrometer Scale," *ACS Nano*, vol. 11, no. 6, pp. 5405–5416, Jun. 2017.

[12]   S. Tawfick *et al.*, "Engineering of micro- and nanostructured surfaces with anisotropic geometries and properties," *Adv. Mater.*, vol. 24, no. 13, pp. 1628–1674, 2012.

[13]   M. De Volder, S. J. Park, S. H. Tawfick, D. O. Vidaud, and A. J. Hart, "Fabrication and electrical integration of robust carbon nanotube micropillars by self-directed elastocapillary densification," *J. Micromech. Microeng.*, vol. 21, p. 045033, 2010.

[14]   M. F. L. De Volder, S. H. Tawfick, R. H. Baughman, and A. J. Hart, "Carbon nanotubes: present and future commercial applications," *Science (80-.).*, vol. 339, no. 6119, pp. 535–539, Feb. 2013.

[15]   M. De Volder, S. H. Tawfick, D. Copic, and A. J. Hart, "Hydrogel-driven carbon nanotube microtransducers," *Soft Matter*, vol. 7, no. 21, pp. 9844–9847, 2011.

[16]   J. Bico, B. Roman, L. Moulin, and A. Boudaoud, "Elastocapillary coalescence in wet hair," *Nature*, vol. 432, no. December, pp. 689–690, 2004.

[17]   M. De Volder and A. J. Hart, "Engineering hierarchical nanostructures by elastocapillary self-assembly," *Angew. Chemie - Int. Ed.*, vol. 52, no. 9, pp. 2412–2425, 2013.

[18] S. Kaur, S. Sahoo, P. Ajayan, and R. S. Kane, "Capillarity-driven assembly of carbon nanotubes on substrates into dense vertically aligned arrays," *Adv. Mater.*, vol. 19, no. 19, pp. 2984–2987, 2007.

[19] S. Jessl, D. Copic, S. Engelke, S. Ahmad, and M. De Volder, "Hydrothermal Coating of Patterned Carbon Nanotube Forest for Structured Lithium-Ion Battery Electrodes," *Small*, p. 1901201, Sep. 2019.

[20] X. Lim, H. W. Gary Foo, G. H. Chia, and C. H. Sow, "Capillarity-assisted assembly of carbon nanotube microstructures with organized initiations," *ACS Nano*, vol. 4, no. 2, pp. 1067–1075, 2010.

[21] C. Py, R. Bastien, J. Bico, B. Roman, and A. Boudaoud, "3D aggregation of wet fibers," *EPL*, vol. 77, p. 44005, 2007.

[22] D. Copic, S. J. Park, S. Tawfick, M. F. L. De Volder, and A. J. Hart, "Fabrication of high-aspect-ratio polymer microstructures and hierarchical textures using carbon nanotube composite master molds," *Lab Chip*, vol. 11, no. 10, pp. 1831–1837, 2011.

[23] A. L. Kaiser, I. Y. Stein, K. Cui, and B. L. Wardle, "Process-morphology scaling relations quantify self-organization in capillary densified nanofiber arrays," *Phys. Chem. Chem. Phys.*, vol. 20, no. 6, pp. 3876–3881, Feb. 2018.

[24] K. Sayama *et al.*, "Photoelectrochemical Decomposition of Water into H and O on Porous BiVO Thin-Film Electrodes under Visible Light and Significant Effect of Ag Ion Treatment Photoelectrochemical Decomposition of Water into H 2 and O 2 on Porous BiVO 4 Thin-Film Electrodes," *J. Phys. Chem. B*, vol. 3, pp. 11352–11360, 2006.

[25] A. Kudo, K. Omori, and H. Kato, "A novel aqueous process for preparation of crystal form-controlled and highly crystalline BiVO4 powder from layered vanadates at room temperature and its photocatalytic and photophysical properties," *J. Am. Chem. Soc.*, vol. 121, no. 49, pp. 11459–11467, 1999.

[26] H. Luo, A. H. Mueller, T. M. McCleskey, A. K. Burrell, E. Bauer, and Q. X. Jia, "Structural and photoelectrochemical properties of BiVO4 thin films," *J. Phys. Chem. C*, vol. 112, no. 15, pp. 6099–6102, 2008.

[27] Y. Ma, S. R. Pendlebury, A. Reynal, F. Le Formal, and J. R. Durrant, "Dynamics of photogenerated holes in undoped BiVO 4 photoanodes for solar water oxidation," *Chem. Sci.*, vol. 5, no. 8, pp. 2964–2973, 2014.

[28] M. Long, W. Cai, and H. Kisch, "Visible light induced photoelectrochemical properties of n-BiVO4 and n-BiVO4/p-Co3O4," *J. Phys. Chem. C*, vol. 112, no. 2, pp.

548–554, 2008.

[29]   J. Gan, X. Lu, and Y. Tong, "Towards highly efficient photoanodes: boosting sunlight-driven semiconductor nanomaterials for water oxidation," *Nanoscale*, vol. 6, no. 13, p. 7142, 2014.

[30]   K. T. Kim *et al.*, "Anatase titania nanorods as an intercalation anode material for rechargeable sodium batteries," *Nano Lett.*, vol. 14, no. 2, pp. 416–422, 2014.

[31]   D. Zhao *et al.*, "Synthesis of carbon-doped BiVO4 @multi-walled carbon nanotubes with high visible-light absorption behavior, and evaluation of their photocatalytic properties," *CrystEngComm*, vol. 18, no. 47, pp. 9007–9015, 2016.

[32]   T. Sun, D. Cui, Q. Ma, X. Peng, and L. Yuan, "Synthesis of BiVO4/MWCNT/Ag@AgCl composite with enhanced photocatalytic performance," *J. Phys. Chem. Solids*, vol. 111, no. March, pp. 190–198, 2017.

[33]   D. Zhao *et al.*, "One-step synthesis of composite material MWCNT@BiVO4 and its photocatalytic activity," *RSC Adv.*, vol. 7, no. 53, pp. 33671–33679, 2017.

[34]   M. F. L. De Volder, D. O. Vidaud, E. R. Meshot, S. Tawfick, and A. J. Hart, "Self-similar organization of arrays of individual carbon nanotubes and carbon nanotube micropillars," *Microelectron. Eng.*, vol. 87, no. 5–8, pp. 1233–1238, 2010.

[35]   S. Tawfick *et al.*, "Mechanics of capillary forming of aligned carbon nanotube assemblies," *Langmuir*, vol. 29, no. 17, pp. 5190–5198, 2013.

[36]   M. Shang, W. Wang, J. Ren, S. Sun, and L. Zhang, "A novel BiVO4 hierarchical nanostructure: controllable synthesis, growth mechanism, and application in photocatalysis," *CrystEngComm*, vol. 12, no. 6, p. 1754, 2010.

[37]   J. B. Liu, H. Wang, S. Wang, and H. Yan, "Hydrothermal preparation of BiVO4 powders," *Mater. Sci. Eng. B Solid-State Mater. Adv. Technol.*, vol. 104, no. 1–2, pp. 36–39, 2003.

[38]   L. Ma, W.-H. Li, and J.-H. Luo, "Solvothermal synthesis and characterization of well-dispersed monoclinic olive-like BiVO4 aggregates," *Mater. Lett.*, vol. 102–103, pp. 65–67, 2013.

[39]   K. Ordon, A. Kassiba, and M. Makowska-Janusik, "Electronic, optical and vibrational features of BiVO 4 nanostructures investigated by first-principles calculations," *RSC Adv.*, vol. 6, no. 112, pp. 110695–110705, 2016.

[40]   A. Zhang and J. Zhang, "Hydrothermal processing for obtaining of BiVO4nanoparticles," *Mater. Lett.*, vol. 63, no. 22, pp. 1939–1942, 2009.

[41]   T. W. Kim and K.-S. Choi, "Nanoporous BiVO4 Photoanodes with Dual-Layer

Oxygen Evolution Catalysts for Solar Water Splitting," *Science (80-.).*, vol. 343, no. February, pp. 990–994, 2014.

[42]   L. Han *et al.*, "Efficient Water-Splitting Device Based on a Bismuth Vanadate Photoanode and Thin-Film Silicon Solar Cells," *ChemSusChem*, vol. 7, no. 10, pp. 2832–2838, Oct. 2014.

[43]   T. W. Kim, Y. Ping, G. A. Galli, and K.-S. Choi, "Simultaneous enhancements in photon absorption and charge transport of bismuth vanadate photoanodes for solar water splitting," *Nat. Commun.*, vol. 6, no. 1, p. 8769, Dec. 2015.

[44]   T. S. Sinclair, B. M. Hunter, J. R. Winkler, H. B. Gray, and A. M. Müller, "Factors affecting bismuth vanadate photoelectrochemical performance," *Mater. Horizons*, vol. 2, no. 3, pp. 330–337, Apr. 2015.